Rapid Flame-Annealed $CuFe_2O_4$ as Efficient Photocathode for Photoelectrochemical Hydrogen Production

Sangwook Park,[†,¶] Ji Hyun Baek,[†,‡,¶] Liang Zhang,[§] Jae Myeong Lee,[‡] Kevin H. Stone,[∥] In Sun Cho,[⊥] Jinghua Guo,[§] Hyun Suk Jung,*[,‡] and Xiaolin Zheng*[,†]

[†]Department of Mechanical Engineering, Stanford University, 440 Escondido Mall, Stanford, California 94305, United States

[‡]School of Advanced Materials Science and Engineering, Sungkyunkwan University, 2066 Seobu-ro, Suwon 16419, Republic of Korea

[§]Advanced Light Source, Lawrence Berkeley National Laboratory, 1 Cyclotron Road, Berkeley, California 94720, United States

[∥]SLAC National Accelerator Laboratory, 2575 Sand Hill Road, Menlo Park, California 94025, United States

[⊥]Department of Materials Science & Engineering and Energy Systems Research, Ajou University, 206 World cup-ro, Suwon 16499, Republic of Korea

ABSTRACT: Copper ferrite ($CuFe_2O_4$) possesses an indirect bandgap in the range of 1.54−1.95 eV. It is used as an attractive *p*-type photocathode in photo-electrochemical (PEC) water splitting, and theoretically it can yield a maximum photocurrent density of ~27 mA/cm^2 and a maximum solar-to-hydrogen conversion efficiency of ~33%. To date, only a few reports have been published on $CuFe_2O_4$ photocathodes with very low-photocurrent densities, with a maximum value of 0.4 mA/cm^2 at 0.4 V vs RHE. Herein, we prepared a $CuFe_2O_4$ photocathode on FTO glass with the sol−gel method followed by either high-temperature flame annealing or furnace annealing. We found that the flame-annealed $CuFe_2O_4$ photocathode generated a photocurrent density of 1.82 mA/cm^2 at 0.4 V vs RHE that is approximately 3.5 times higher than the furnace-annealed $CuFe_2O_4$ (0.52 mA/cm^2). This photocurrent density is also higher than those of all the reported $CuFe_2O_4$ photocathodes, and any Cu containing ternary oxide (Cu−M−O, M: Fe, Bi, V, and Nb) photocathode (0.1−1.3 mA/cm^2 at 0.4 V vs RHE). An improved PEC performance of the flame-annealed $CuFe_2O_4$ photocathode is elicited owing to the beneficial effects of flame annealing on the physical, optical, and electrical properties of $CuFe_2O_4$. Flame annealing enhances the light absorption property of the $CuFe_2O_4$ photocathode by slightly reducing the bandgap, and by forming a thicker film with increased porosity. Flame annealing also reduces the oxygen vacancy concentration in $CuFe_2O_4$, thus facilitating charge transport and interfacial charge transfer processes. Moreover, flame annealing requires only 16 min, which is much shorter than the time required for furnace annealing (~9 h). These results demonstrate that flame annealing is a rapid and effective means for fabricating metal oxide photoelectrodes with an enhanced PEC water splitting performance.

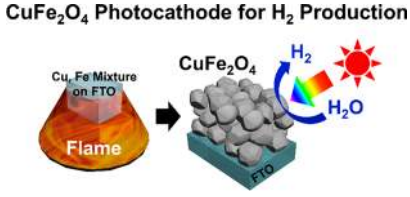

INTRODUCTION

Photoelectrochemical (PEC) water splitting has been extensively studied as a possible hydrogen production technique that utilizes solar energy to split water.[1−3] A potential bias-free PEC configuration could be represented by the tandem cell that consists of *p*-type photocathodes and *n*-type photoanodes.[1,4−7] There is a general consensus for inexpensive, active, and stable *n*-type photoanode materials, such as $BiVO_4$,[8,9] WO_3,[10,11] Fe_2O_3,[12,13] and TiO_2.[14,15] In comparison, there is lack of suitable *p*-type photocathode candidates.[16,17] Good candidates for photocathodes are copper-based metal oxides because they are mostly nontoxic and cost-effective. For example, CuO[18,19] and Cu_2O[20−22] photocathodes have been used for PEC water reduction and have elicited good performance but poor stability. In addition, $CuFeO_2$,[23−25] $CuBi_2O_4$,[26,27] Cu_3VO_4,[28] and $CuNb_2O_6$[29] photocathodes have been shown to have modest performance and stability.

Copper ferrite ($CuFe_2O_4$) is another *p*-type semiconductor in the family of copper-based metal oxides. $CuFe_2O_4$ has several attractive properties that makes it a possible candidate for photocathodes. $CuFe_2O_4$ has a narrow indirect bandgap in the range of 1.54−1.95 eV, thus yielding a theoretical maximum photocurrent density of ~27 mA/cm,[2] and a maximum solar-to-hydrogen conversion efficiency of ~33%.[30−34] $CuFe_2O_4$ has a conduction band minimum that is suitable for hydrogen evolution reactions.[3,26] In fact, several studies have tested $CuFe_2O_4$ in photocathodes for PEC hydrogen evolution, but its elicited performance has been poor.[31,32,35−37] Diez-Garcia et al. coated commercial, cubic $CuFe_2O_4$ nanoparticles with 30 nm which possessed a high-

Table 1. Summary of Various Cu-Based Ternary Oxide Photocathodes

	J_{ph} @ 0.4 V_{RHE} (mA/cm^2)	J_{dark} @ 0.4 V_{RHE} (mA/cm^2)	V_{onset} (V_{RHE})	electrolyte	thickness	stability[d]	ref
$CuFe_2O_4$ (flame)	−1.82	−0.35	1.05	Ar purged 1 M NaOH	530 nm	600s @ 0.15 V_{RHE} in Ar purged 1 M Na_2SO_4	this work
$CuFe_2O_4$ (furnace)	−0.52	−0.15	0.85	Ar purged 1 M NaOH	450 nm	450s @ 0.15 V_{RHE} in Ar purged 1 M Na_2SO_4	this work
$CuFe_2O_4$	−0.04[a]	∼0	1.1	N_2 purged 0.1 M NaOH	14 μm	–	32
$CuFe_2O_4$	−0.4	−0.25	0.5	0.2 M Na_2SO_4	60 nm NPs	over 240 s @ −0.2 V_{SCE}	36
$CuFeO_2$	−1.25	−0.25	0.9	O_2 purged 1 M NaOH	290 nm	over 600 s[e]	23
$CuFeO_2$	−0.3	−0.1	0.81	Ar purged 1 M NaOH	130 nm	70s @ 0.6 V_{RHE}	24
$CuFeO_2$	−1.3	−0.2	0.8	Ar purged 1 M NaOH	6 times spin coating	20 min w/NiFe/RGO in Ar purged 1 M NaOH	25
$CuBi_2O_4$	−0.8[b]	∼0	1.25	1 M NaOH	over 1 μm	over 1 h @ 0.6 V_{RHE}	26
Cu_3VO_4	−0.77[c]	−0.55	0.2 V_{SCE}	0.5 M Na_2SO_4	1 μm	250s w/CuO NPs	28
$CuNb_2O_6$	−0.25	−0.1	0.78	CO_2 purged 0.1 M $NaHCO_3$	20 nm NPs	–	29

[a]At −0.2 V vs Ag/AgCl. [b]At 0.6 V vs RHE. [c]At −0.18 V vs SCE. [d]Time for J_{ph} to be halved from its initial value. [e]With AZO/TiO_2/Pt @ 0 V_{RHE} in Ar purged 0.5 M Na_2SO_4.

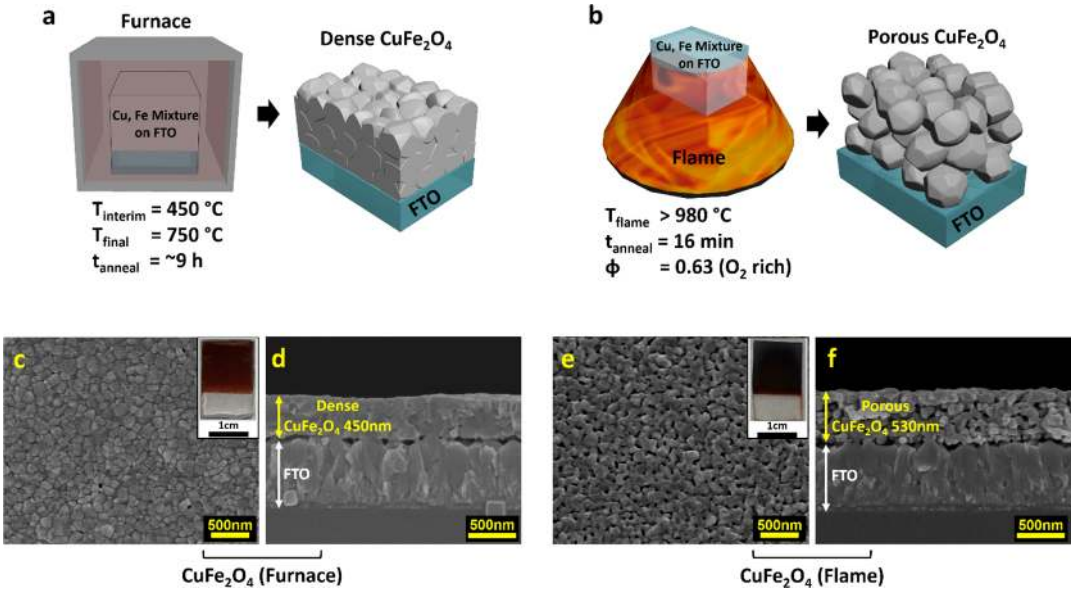

Figure 1. Schematic of $CuFe_2O_4$ on FTO annealed by furnace and flame. (a) Illustration of the furnace annealing conditions and the dense film structure of the $CuFe_2O_4$ (furnace) on FTO. (b) Illustration of the flame annealing conditions and the porous film structure of the flame-annealed $CuFe_2O_4$ on FTO. (c, d) SEM images of top (c) and cross (d) view of $CuFe_2O_4$ on FTO (furnace). (e, f) SEM images of top (e) and cross (f) view of $CuFe_2O_4$ on FTO (flame).

degree of crystallinity on fluorine-doped tin oxide (FTO) glass substrate, followed by annealing at 450 °C for 1 h and electrochemical pretreatment. This $CuFe_2O_4$ photocathode finally attained a film thickness of 14 μm and achieved a current density of −40 $\mu A/cm^2$ at 0.75 V vs RHE.[32] Li et al. grew cubic spinel structure of $CuFe_2O_4$ nanoparticle with average diameters in the range of 50−60 nm using the hydrothermal method followed by the coating of the particles on FTO and annealing at 400 °C for 2 h. This $CuFe_2O_4$ photocathode has a PEC performance of −0.4 mA/cm^2 at 0.4 V vs RHE.[36] Among the various factors that account for the poor performances of these $CuFe_2O_4$ photocathodes was the poor contact between $CuFe_2O_4$ and FTO, as $CuFe_2O_4$ was coated on FTO with moderate post sintering temperature in the range of 400−450 °C. Better interface can be achieved by directly growing $CuFe_2O_4$ on the FTO substrate. The challenge is attributed to the fact that the crystallization temperature of $CuFe_2O_4$ (800−1000 °C) is much higher than the glass transition temperature of FTO (∼564 °C).

Herein, we apply our rapid and high-temperature flame annealing method (>980 °C)[12,14,15,38−40] to anneal $CuFe_2O_4$ precursor films coated on FTO glass to prepare $CuFe_2O_4$ photocathode with high crystallinity and good contact with FTO glass. For comparison, we also prepared a control sample of a $CuFe_2O_4$ film which was coated on FTO glass after it was annealed in a conventional box furnace at 750 °C. The flame-annealed $CuFe_2O_4$ photocathode elicited a photocurrent density which was ∼3.5 times higher (−1.82 mA/cm^2 E) than that of furnace-annealed $CuFe_2O_4$ (−0.52 mA/cm^2) at 0.4 V vs RHE under 1 sun illumination in Ar purged 1 M NaOH electrolyte. The enhanced PEC performance of the flame-annealed $CuFe_2O_4$ photocathode was attributed to several reasons, as described next. First, flame annealing makes the $CuFe_2O_4$ film more porous and thicker that

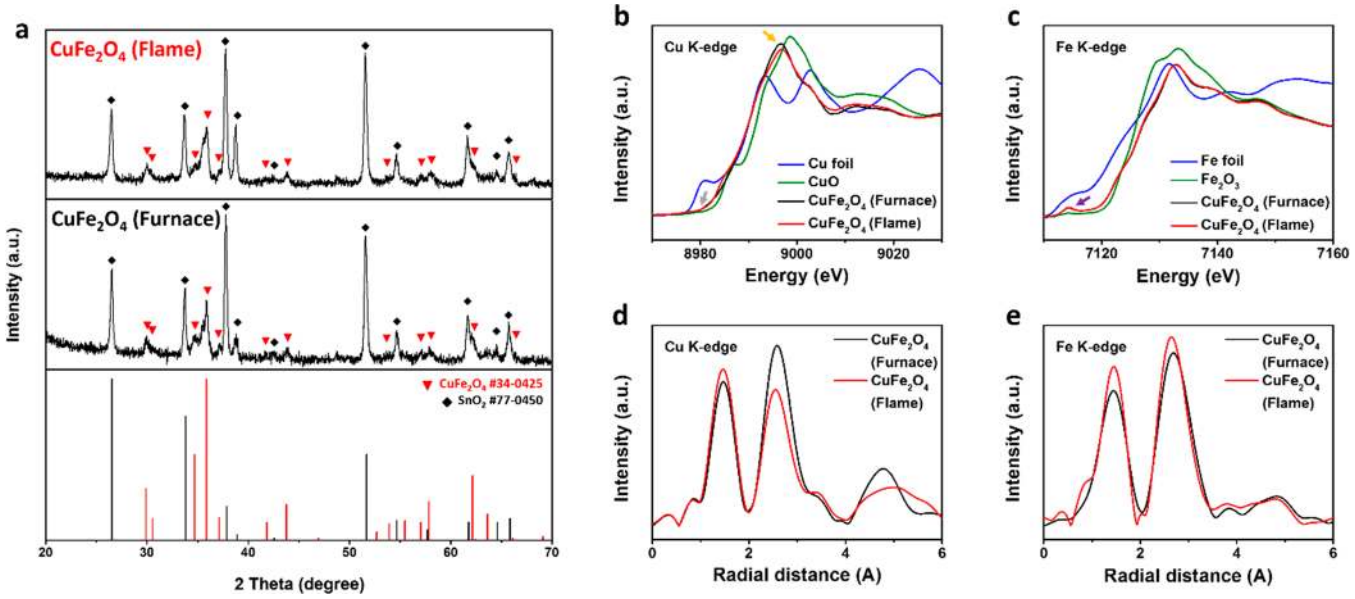

Figure 2. X-ray diffraction (XRD) and X-ray absorption spectroscopy (XAS) characterization on $CuFe_2O_4$ annealed by furnace and flame. (a) XRD spectra of $CuFe_2O_4$ film on FTO annealed by flame (top) and furnace (middle). Corresponding peaks signals of $CuFe_2O_4$ (red) and FTO (black) from the JCPDS database are shown in the bottom figure. (b, c) Cu K-edge (b) and Fe K-edge (c) X-ray absorption near-edge structure (XANES) spectra of $CuFe_2O_4$ by furnace (black solid) and flame (red solid). (d, e) Cu K-edge (d) and Fe K-edge (e) extended X-ray absorption fine structure (EXAFS) functions of $CuFe_2O_4$ by furnace (black solid) and flame (red solid).

increases light absorption in the visible light region (400−700 nm), and increases the surface area.[41−43] Second, flame-annealed $CuFe_2O_4$ has fewer oxygen vacancies, thus leading to more efficient charge transport and transfer processes. Third, flame-annealed $CuFe_2O_4$ has a slightly smaller optical bandgap that extends the range of light absorption. Additionally, the flame annealing method shortens the annealing time from ∼9 h to 16 min. To the best of our knowledge, the photocurrent density of our flame-annealed $CuFe_2O_4$ is higher than all the reported Cu-based ternary oxide photocathodes (Table 1).

EXPERIMENTAL SECTION

Synthesis of $CuFe_2O_4$ Film on FTO Substrate by Flame and Furnace. All samples were prepared on fluorine-doped tin oxide (FTO) coated-glass substrates (TEC 7, 7−8 Ω/sq, MSE Supplies). The FTO substrates were cleaned in acetone, IPA, and DI water, with sonication for 15 min, and were dried by an air gun. The $CuFe_2O_4$ precursor was prepared by the sol−gel method and was spin-coated on FTO glass for both annealing methods (see Supporting Information) at 3000 rpm for 60 s. The samples were then dried on a hot plate at 100 °C for 10 min. For furnace annealing (Figure 1a), the samples were annealed in a box furnace at 450 °C in air for 1 h after each spin coating, and the optimized thickness was achieved after five spin coatings. The samples are finally annealed at 750 °C for 20 min. For flame annealing (Figure 1b), the samples were annealed in an oxygen-rich postflame region at 980 °C for 2 min after each spin coating until all the five layers were optimized, followed by the final annealing at 980 °C for 8 min. Flame annealing was employed using a coflow premixed flat flame burner (McKenna Burner).[12,14,15,38−40] The flow rates of CH_4 and air were set to 2.05 and 31.3 SLPM so that the fuel to oxygen equivalence ratio (Φ) was 0.63.

Photoelectrochemical Characterization. The PEC performances were measured in a standard three-electrode PEC cell using a Gamry 1000 potentiostat.[44] The $CuFe_2O_4$ samples were used as the working electrodes with a glassy carbon as the counter electrode and Ag/AgCl reference electrode. Argon purged 1 M sodium hydroxide (NaOH) electrolyte (pH ∼ 13.5) was used in all PEC measurements if not specified otherwise. All the PEC measurements were performed by employing a solar simulator (Model LCS-100, Newport), and the intensity was calibrated for a standard 1 sun condition (AM 1.5 G, 100 mW/cm^2) using a photovoltaic reference (Model 91150 V, Newport). Electrochemical impedance spectroscopy (EIS) measurements were performed in the same, standard three-electrode configuration, using a potentiostat (SP−200, Biologic) using 1 sun illumination. The incident photon-to-current conversion efficiency (IPCE) was measured at 0.4 V vs RHE with the use of a 150 W xenon arc lamp source (ABET Technologies) and a monochromator (Mmac 200, 600 gr/mm blazed at 500 nm) with a standard silicon photodiode cell.

RESULTS AND DISCUSSION

Methodological Differences between Furnace and Flame Annealing. As shown in Figure 1a,b, the main differences between furnace and flame annealing methods are the annealing temperature and duration. There is an upper annealing temperature limit for FTO glass as its glass transition temperature is approximately 564 °C,[38] and its conductivity decreases when annealed at a temperature above 800 °C.[45,46] Furnace annealing provides a homogeneous temperature environment, and our test shows that furnace annealing at 750 °C for 20 min is the upper temperature limit before severe FTO sheet resistance effects are documented. In contrast, many of our previous studies have demonstrated that flame annealing provides a heterogeneous temperature field. The coated materials on FTO (e.g., $CuFe_2O_4$ precursors) are exposed to high temperature but most of FTO glass is kept at a lower temperature due to large spatial temperature gradient, thus protecting its integrity and conductivity.[14,15,38−40] The sheet resistances of FTO before and after flame annealing are close to the pristine value provided by vendor (Figure S1), confirming little impact on FTO from flame annealing. In addition, flame annealing not only enables the use of higher temperatures but also allows negligible ramping/cooling rates compared to the furnace. Therefore, flame annealing dramatically reduces the annealing time from ∼9 h (furnace) to 16 min (flame).

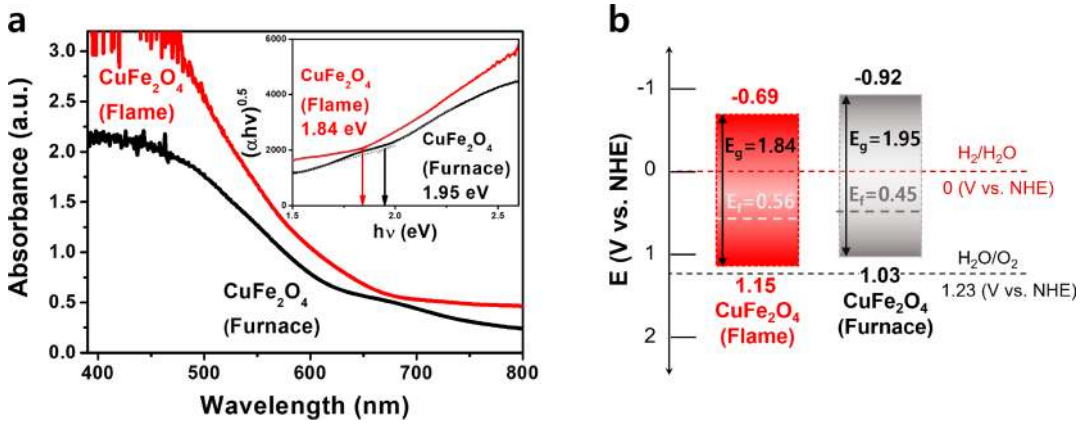

Figure 3. UV−vis spectra and energy band positions of $CuFe_2O_4$ annealed by furnace and flame. (a) UV−vis spectra and the corresponding Tauc plots for indirect bandgaps shown in insets. The corresponding Tauc plots for direct bandgaps are shown in Figure S4. (b) Comparison of the energy band positions for $CuFe_2O_4$ annealed by furnace and flame in contact with aqueous electrolyte at pH 0.

Morphological Comparison of $CuFe_2O_4$ Photocathodes Annealed by Furnace and Flame. We first investigated how the furnace and flame annealing methods affect the morphology of $CuFe_2O_4$ thin films coated on FTO glass. SEM images show the morphology of the $CuFe_2O_4$ film annealed by furnace (Figure 1c,d) and flame (Figure 1e,f). The $CuFe_2O_4$ (furnace) film is very dense (~450 nm) with connected grains, while the $CuFe_2O_4$ (flame) is porous and thicker (~530 nm). The greater porosity and thickness of the $CuFe_2O_4$ (flame) enhances its light absorption response and increases its contact area with the electrolyte, yet both factors improve the PEC performance, as discussed below.

X-ray Characterizations of $CuFe_2O_4$ Annealed by Furnace and Flame. The crystallinity of $CuFe_2O_4$ (flame and furnace) film was examined by X-ray diffraction (XRD) as shown in Figure 2a. The XRD data of both $CuFe_2O_4$ films match the standard $CuFe_2O_4$ spectra (JCPDS, #34-0425), thus confirming the successful crystallization of the tetragonal copper ferrite phase that is a extensively used as the structural phase for high-performance photocatalysts.[32] Figure S2 shows that the $CuFe_2O_4$ phase, which annealed at 450 °C for 1 h, is amorphous, thus confirming the need for high-temperature annealing for its crystallization.

To better understand the chemical states of $CuFe_2O_4$ (flame and furnace), we performed Cu and Fe K-edge X-ray absorption near-edge structure (XANES) experiments. The Cu K-edge XANES spectra of $CuFe_2O_4$ synthesized by furnace and flame annealing are shown along with the reference sample spectra of Cu foil and CuO in Figure 2b. The spectra of both $CuFe_2O_4$ samples show a peak at 8,997 eV (orange arrow) and have an edge rising position of ~8,980 eV (gray arrow), thus indicating the absence of Cu^{1+} cations and the occupancy of the octahedral sites of Cu^{2+} cations.[25,47] The Fe K-edge XANES spectra of both $CuFe_2O_4$ samples (Figure 2c) yielded a pre-edge peak at 7,114 eV (purple arrow), which is the characteristic feature of Fe^{3+} cations in the tetrahedral sites.[47] The pre-edge peak is attributed to the transition from 1s to 3d, which is dipole-forbidden for the absorbers in a centrosymmetric environment.[48] The enhancement of the pre-edge peak in the Fe K-edge XANES spectra is owing to the breaking of the symmetry owing to the noncentrosymmetric tetrahedral crystal field of Fe^{3+} cations in $CuFe_2O_4$.

The XANES spectra analysis revealed a minor difference between flame- and furnace-annealed $CuFe_2O_4$ samples. We then performed extended X-ray absorption fine structure (EXAFS) measurements to compare the local atomic structure of $CuFe_2O_4$ (flame and furnace). Figure 2d,e shows the Fourier transformed (FT) curves of Cu and Fe K-edge EXAFS spectra, respectively. For the Cu K-edge FT curves, the first peak at 1.45 Å originates from the Cu−O bond,[47,49] and the second peak at 2.57 Å is ascribed to the bonds of Cu−Fe and Cu−Cu with both cations occupying the octahedral sites.[47,49] The $CuFe_2O_4$ (flame) elicits a higher intensity for the first peak (Cu−O bond), while the $CuFe_2O_4$ (furnace) has a higher intensity for the second peak (Cu−Fe and Cu−Cu bonds). This difference suggests that the $CuFe_2O_4$ (flame) has fewer oxygen vacancies.[50] The Fe K-edge results yielded a similar behavior in that $CuFe_2O_4$ (flame) shows a higher relative intensity for the first peak (Fe−O bond) than the second peak (Fe−Cu and Fe−Fe) compared with those of $CuFe_2O_4$ (furnace).[47,49] The difference in the oxygen vacancy between $CuFe_2O_4$ films by flame and furnace is expected to affect their electronic properties and performance for PEC hydrogen production (Figure S3).

Electronic Band Structure Comparison of $CuFe_2O_4$ Annealed by Furnace and Flame. The electronic structures of the $CuFe_2O_4$ (flame and furnace) films were investigated by UV−vis spectroscopy and ultraviolet photoelectron spectroscopy (UPS). The UV−vis spectroscopy determined the band gap from the Tauc plot method (Figure 3a). The Tauc plots show that both $CuFe_2O_4$ (flame and furnace) films have an indirect bandgap, as shown in the inset of Figure 3a. The $CuFe_2O_4$ (flame) has a slightly smaller optical bandgap (1.84 eV) than that of $CuFe_2O_4$ (furnace, 1.95 eV). The $CuFe_2O_4$ (flame) and $CuFe_2O_4$ (furnace) have theoretical photocurrent density limits of ~17.5 and ~15.3 mA/cm^2, respectively, which were calculated based on reference solar spectral irradiances (AM1.5, ASTM G173, NREL). The bandgap values are close to the previously reported bandgap range of $CuFe_2O_4$ from 1.54 to 1.80 eV.[30−33] Moreover, the $CuFe_2O_4$ (flame) had a higher light absorption efficiency than $CuFe_2O_4$ (furnace) over the wavelength range from 400 to 700 nm (Figure S5), which is a consequence of its higher porosity and thickness (Figure 1c−f).

The UPS measurement (Figure S6) was used to determine the work function and the valence band maximum (VBM) of $CuFe_2O_4$. The band positions and band edge values for $CuFe_2O_4$ (flame and furnace) were estimated by UPS

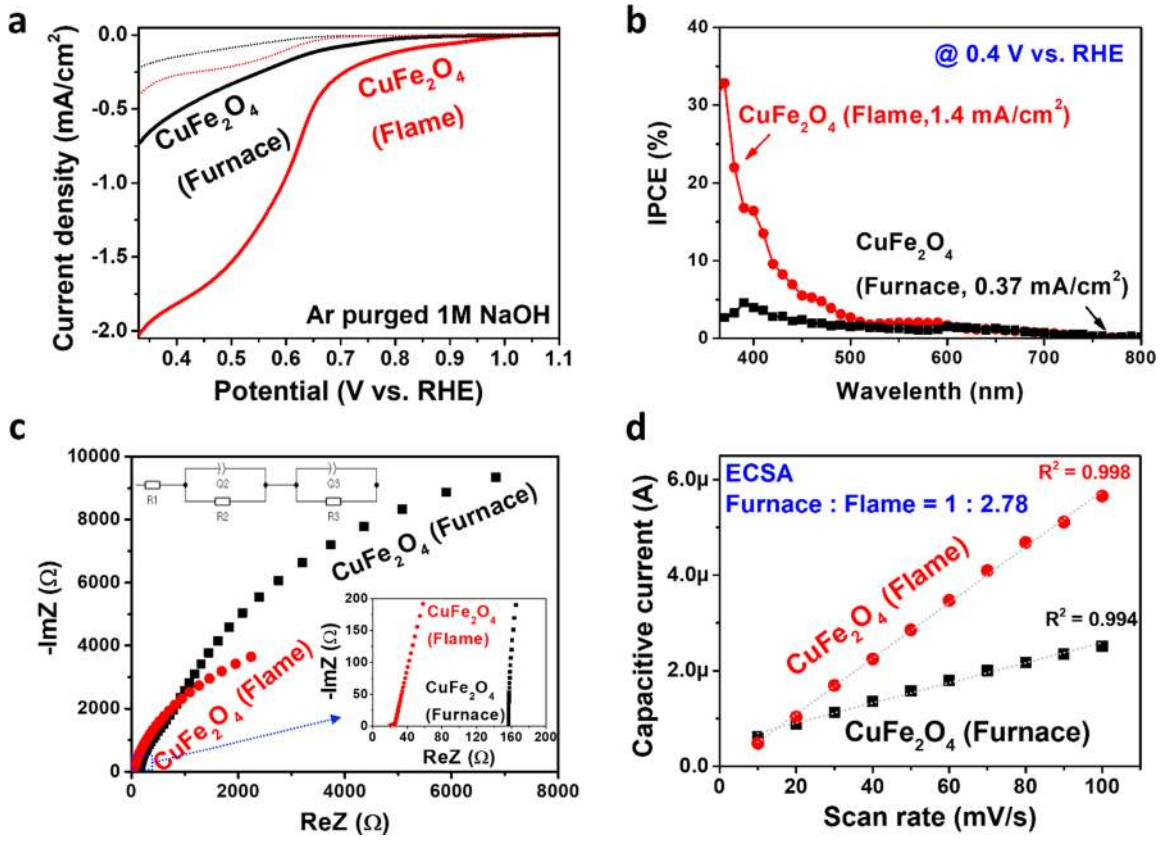

Figure 4. Photoelectrochemical (PEC) characterizations on $CuFe_2O_4$ photocathode by furnace and flame. (a) $J-V$ curves of $CuFe_2O_4$ photocathode measured in Ar purged 1 M NaOH under simulated 1 sun illumination (100 mW/cm^2) for hydrogen production. The scan rate was 10 mV/s and the scan direction was in cathodic sweep. (b) Incident photon to current efficiency (IPCE) of $CuFe_2O_4$ photocathode. (c) Electrochemical impedance spectra (EIS) of $CuFe_2O_4$ photocathode at 0.4 V vs RHE under simulated 1 sun illumination. (d) Capacitive currents measured at 1.13 V vs RHE as a function of scan rate for the relative electrochemical active surface area (ECSA) measurements. In all figures, $CuFe_2O_4$ (Furnace) is black and $CuFe_2O_4$ (Flame) is red.

measurements, as shown in Figure 3b. According to the UPS and UV−vis data, the calculated conduction band minimum values of $CuFe_2O_4$ (flame and furnace) films are −0.69 and −0.92 V vs NHE, and the maximum values of the valence band are 1.15 and 1.03 V vs NHE, respectively (see the Experimental Section for details). The obtained band structures confirmed that the $CuFe_2O_4$ photocathodes synthesized by flame and furnace annealing were thermodynamically favorable to drive the hydrogen evolution reaction.[26]

Photoelectrochemical Characterizations of $CuFe_2O_4$ Annealed by Furnace and Flame. Figure 4a shows the linear sweep voltammetry of $CuFe_2O_4$ (flame and furnace) in Ar purged 1 M NaOH electrolyte in the dark (dashed lines), and under 1 sun illumination (solid lines). These polarization curves were constructed with a scan rate of 10 mV/s. Correspondingly, the current density values were calculated based on the projected area of the FTO glass substrate. The thickness of the $CuFe_2O_4$ film had been optimized based on the photocurrent density values under 1 sun illumination (Figure S7). The optimal thickness is shown in Figure 1d,f.

The $CuFe_2O_4$ (flame) clearly elicited a better PEC performance than $CuFe_2O_4$ (furnace) with an earlier onset and a higher photocurrent density in the range of the voltage sweep. The $CuFe_2O_4$ (flame) photocathode exhibited a positively shifted onset potential of ∼1.05 V vs RHE, in comparison to that of the $CuFe_2O_4$ (furnace) of ∼0.85 V vs RHE. This characteristic establishes the $CuFe_2O_4$ (flame) as a better photocathode for coupling with the photoanode in a PEC tandem cell.[3,26] The photocurrent density of $CuFe_2O_4$ (flame, −1.82 mA/cm^2) is ∼3.5 times higher than that of $CuFe_2O_4$ (furnace, −0.52 mA/cm^2) at 0.4 V vs RHE under 1 sun illumination. We noted that the photocurrent density for $CuFe_2O_4$ (flame) has a step change at ∼0.65 V vs RHE, and this step change is reduced by increasing the scan rate (>10 mV/s, Figure S8). These results indicate the presence of surface states for $CuFe_2O_4$ (flame) and they contribute to surface recombination. Figure 4b shows the incident photon-to-current conversion efficiency (IPCE) data of $CuFe_2O_4$ (flame and furnace) photocathodes at 0.4 V vs RHE. The integrated photocurrent densities from IPCE are 1.40 and 0.36 mA/cm^2 for $CuFe_2O_4$ (flame) and $CuFe_2O_4$ (furnace) respectively, and are lower than the light J_{ph} but consistent with the values of $(J_{ph} - J_{dark})$ at 0.4 V vs RHE in the $J-V$ plot (Figure 4a). This suggests that side reactions occur, even in the dark, which could be attributed to the exposure of the FTO substrate and the instability of copper-based oxides. Similar dark currents are also commonly observed for copper-containing photocathodes, as listed in Table 1. Importantly, the photocatalytic activity of $CuFe_2O_4$ (flame) is the best among the recently reported Cu- and Fe-based ternary oxides for the photocathode, as characterized by the photocurrent density at 0.4 V vs RHE (Table 1).

The improved PEC performance of $CuFe_2O_4$ (flame) photocathode is only partially caused by its enhanced light

absorption property in the visible light region (Figure S5) owing to its thicker and more porous film morphology. In addition, we further conducted electrochemical impedance spectroscopic (EIS) analyses to compare the effect of furnace and flame annealing on the charge transport and transfer efficiency. The EIS data were measured at 0.4 V vs RHE under 1 sun illumination were fitted to a circuit model, as specified in an inlet of Figure 4c. In this model, the resistances and capacitances are composed of a series resistance (R1) that describes the charge transport resistance at the interface between the $CuFe_2O_4$ film and the FTO substrate, a charge transport resistance (R2) and a capacitance of the space charge region (C2) in the bulk of material, and a charge transfer resistance (R3) and a Helmholtz capacitance (C3) at the interface between the $CuFe_2O_4$ film and the liquid electrolyte.[51] The fitted resistance values are listed in Table 2. First,

Table 2. Resistances of Each Material Measured by EIS Shown in Figure 4c

Unit [Ω]	R1	R2	R3
$CuFe_2O_4$ (furnace)	156.8	19989	666.9
$CuFe_2O_4$ (flame)	19.46	10962	6.037

the flame-annealed film has a better electrical contact between the $CuFe_2O_4$ film and the FTO substrate since the values of R1 of flame-annealed $CuFe_2O_4$ (19.46 Ω) is much smaller than that of furnace-annealed $CuFe_2O_4$ (156.8 Ω). In addition, the charge transport resistance of $CuFe_2O_4$ (flame) is lower (~11 kΩ) than that of $CuFe_2O_4$ (furnace, ~20 kΩ). This is attributed to the reduced oxygen vacancies from the EXAFS analysis in Figure 2d,e.[52] Moreover, the charge injection resistance was dramatically reduced from ~667 Ω for $CuFe_2O_4$ (furnace) to ~6 Ω for $CuFe_2O_4$ (flame). The EIS results indicate that flame annealing improves both the charge transfer and transport efficiencies, thus leading to the enhanced PEC performance of $CuFe_2O_4$ (flame).

Additionally, we measured the electrochemical active surface area (ECSA) to understand the charge transfer process. The capacitive currents were measured at 1.13 V vs RHE because there was no noticeable Faradaic current in the potential range from 0.78 to 1.18 V vs RHE. Figure 4d plots the capacitive current as a function of scan rate for $CuFe_2O_4$ (flame and furnace) in which the slope is proportional to the ECSA ratio.[53] The ECSA ratio of the $CuFe_2O_4$ based on flame and furnace is 2.78. The higher ECSA value of $CuFe_2O_4$ (flame) indicates a better interfacial charge transfer efficiency, which is consistent with the EIS results (Figure 4c).

Finally, the stability of the $CuFe_2O_4$ photocathode was tested using chronoamperometry using chopped illumination at 0.15 V vs RHE for 10 min in Ar purged 1 M Na_2SO_4 electrolyte in agreement with the $J-V$ curves (Figure S9). The stability test was not conducted in 1 M NaOH but in 1 M Na_2SO_4 to reduce the chemical influence from the strong alkaline electrolytes. Both $CuFe_2O_4$ films by flame (red) and furnace (black) show acceptable stabilities, as compared to many reported Cu- and Fe-based ternary oxides (Table 1)[23,25] and Cu_2O[20] without the use of any protective layers and electrocatalyst.[21,54,55] The stability of the $CuFe_2O_4$ photocathode still needs to be further improved to be a practical photocathode. The main reason for the instability is the chemical reduction of Cu^{2+} under the PEC bias range needed for hydrogen evolution reaction (Figures S10–S12). Potential methods for improving the stability of the $CuFe_2O_4$ include elemental doping, deposition of protection layers, addition of electrocatalysts, and a combination of them.

CONCLUSIONS

In summary, we investigated the potential of flame-annealed $CuFe_2O_4$ as a photocathode for PEC hydrogen production. The flame-annealed $CuFe_2O_4$ photocathode achieved a photocurrent density of −1.82 mA/cm^2 at 0.4 V vs RHE that is higher than the photocurrent density of the furnace-annealed $CuFe_2O_4$, and the corresponding photocurrent density values of all the reported Cu-based ternary oxide photocathodes. The enhanced PEC performance of the flame-annealed $CuFe_2O_4$ photocathode was attributed to several factors. First, the flame-annealed $CuFe_2O_4$ film was more porous and thicker, and led to a better light absorption and a higher surface area. Second, the flame-annealed $CuFe_2O_4$ had fewer oxygen vacancies, and hence achieved more efficient charge transport and transfer processes. Third, flame-annealed $CuFe_2O_4$ had a slightly smaller optical bandgap that extended the range of light absorption. On top of that, the flame annealing method shortened the annealing time from ~9 h to 16 min. These results showed that the $CuFe_2O_4$ photocathode could elicit a good performance for PEC hydrogen production. Nevertheless, the stability of the $CuFe_2O_4$ photocathode is still not adequate and it has to be further improved for practical PEC water splitting.

AUTHOR INFORMATION

Corresponding Authors

*S. Jung. E-mail: hsjung1@skku.edu. Fax: +82-31-290-7410. Phone: +82-31-290-7403.

*X. Zheng. E-mail: xlzheng@stanford.edu. Fax: +1-650-723-1748. Phone: +1-650-736-8953.

ORCID

Sangwook Park: 0000-0003-0939-1696

Liang Zhang: 0000-0002-3446-3172

In Sun Cho: 0000-0001-5622-7712

Jinghua Guo: 0000-0002-8576-2172

Hyun Suk Jung: 0000-0002-7803-6930

Xiaolin Zheng: 0000-0002-8889-7873

Author Contributions

[¶]These authors contributed equally to this work.

Notes

The authors declare no competing financial interest.

■ ACKNOWLEDGMENTS

X.Z. acknowledges generous financial support from the Stanford Woods Institute for the Environment and the Stanford Natural Gas Initiative for their generous support. This work was also supported by Basic Science Research Program through the National Research Foundation of Korea (No. 2017R1A2B3010927), Global Frontier R&D Program of the Center for Multiscale Energy System (2012M3A6A7054855), and Creative Materials Discovery Program (2016M3D1A1027664). Use of the Stanford Synchrotron Radiation Lightsource, SLAC National Accelerator Laboratory, is supported by the U.S. Department of Energy, Office of Science, Office of Basic Energy Sciences under Contract No. DE-AC02-76SF00515. J.G. used resources on BL8.0.1 of the Advanced Light Source, which is a DOE Office of Science User Facility under contract no. DE-AC02-05CH11231.

■ REFERENCES

(1) Chu, S.; Li, W.; Yan, Y.; Hamann, T.; Shih, I.; Wang, D.; Mi, Z. Roadmap on solar water splitting: current status and future prospects. *Nano Futures* **2017**, *1* (2), 022001.

(2) Tachibana, Y.; Vayssieres, L.; Durrant, J. R. Artificial photosynthesis for solar water-splitting. *Nat. Photonics* **2012**, *6* (8), 511−518.

(3) Walter, M. G.; Warren, E. L.; McKone, J. R.; Boettcher, S. W.; Mi, Q.; Santori, E. A.; Lewis, N. S. Solar water splitting cells. *Chem. Rev.* **2010**, *110*, 6446−6473.

(4) Prévot, M. S.; Sivula, K. Photoelectrochemical Tandem Cells for Solar Water Splitting. *J. Phys. Chem. C* **2013**, *117* (35), 17879−17893.

(5) Jang, Y. J.; Jeong, I.; Lee, J.; Lee, J.; Ko, M. J.; Lee, J. S. Unbiased Sunlight-Driven Artificial Photosynthesis of Carbon Monoxide from CO_2 Using a ZnTe-Based Photocathode and a Perovskite Solar Cell in Tandem. *ACS Nano* **2016**, *10* (7), 6980−6987.

(6) Abdi, F. F.; Han, L.; Smets, A. H.; Zeman, M.; Dam, B.; van de Krol, R. Efficient solar water splitting by enhanced charge separation in a bismuth vanadate-silicon tandem photoelectrode. *Nat. Commun.* **2013**, *4*, 2195.

(7) Zhang, K.; Ma, M.; Li, P.; Wang, D. H.; Park, J. H. Water Splitting Progress in Tandem Devices Moving Photolysis beyond Electrolysis. *Adv. Energy Mater.* **2016**, *6*, 1600602.

(8) Han, H. S.; Shin, S.; Kim, D. H.; Park, I. J.; Kim, J. S.; Huang, P.-S.; Lee, J.-K.; Cho, I. S.; Zheng, X. Boosting the solar water oxidation performance of a $BiVO_4$ photoanode by crystallographic orientation control. *Energy Environ. Sci.* **2018**, *11* (5), 1299−1306.

(9) Baek, J. H.; Kim, B. J.; Han, G. S.; Hwang, S. W.; Kim, D. R.; Cho, I. S.; Jung, H. S. $BiVO_4/WO_3/SnO_2$ Double-Heterojunction Photoanode with Enhanced Charge Separation and Visible-Transparency for Bias-Free Solar Water-Splitting with a Perovskite Solar Cell. *ACS Appl. Mater. Interfaces* **2017**, *9* (2), 1479−1487.

(10) Rao, P. M.; Cho, I. S.; Zheng, X. Flame synthesis of WO_3 nanotubes and nanowires for efficient photoelectrochemical water-splitting. *Proc. Combust. Inst.* **2013**, *34* (2), 2187−2195.

(11) Yoon, H.; Mali, M. G.; Kim, M.-w.; Al-Deyab, S. S.; Yoon, S. S. Electrostatic spray deposition of transparent tungsten oxide thin-film photoanodes for solar water splitting. *Catal. Today* **2016**, *260*, 89−94.

(12) Cho, I. S.; Han, H. S.; Logar, M.; Park, J.; Zheng, X. Enhancing Low-Bias Performance of Hematite Photoanodes for Solar Water Splitting by Simultaneous Reduction of Bulk, Interface, and Surface Recombination Pathways. *Adv. Energy Mater.* **2016**, *6* (4), 1501840.

(13) Kim, J. Y.; Youn, D. H.; Kang, K.; Lee, J. S. Highly Conformal Deposition of an Ultrathin FeOOH Layer on a Hematite Nanostructure for Efficient Solar Water Splitting. *Angew. Chem., Int. Ed.* **2016**, *55* (36), 10854−10858.

(14) Cho, I. S.; Lee, C. H.; Feng, Y.; Logar, M.; Rao, P. M.; Cai, L.; Kim, D. R.; Sinclair, R.; Zheng, X. Codoping titanium dioxide nanowires with tungsten and carbon for enhanced photoelectrochemical performance. *Nat. Commun.* **2013**, *4*, 1723.

(15) Cho, I. S.; Logar, M.; Lee, C. H.; Cai, L.; Prinz, F. B.; Zheng, X. Rapid and controllable flame reduction of TiO_2 nanowires for enhanced solar water-splitting. *Nano Lett.* **2014**, *14* (1), 24−31.

(16) Kang, D.; Kim, T. W.; Kubota, S. R.; Cardiel, A. C.; Cha, H. G.; Choi, K. S. Electrochemical Synthesis of Photoelectrodes and Catalysts for Use in Solar Water Splitting. *Chem. Rev.* **2015**, *115* (23), 12839−12887.

(17) Jiang, C.; Moniz, S. J. A.; Wang, A.; Zhang, T.; Tang, J. Photoelectrochemical devices for solar water splitting - materials and challenges. *Chem. Soc. Rev.* **2017**, *46* (15), 4645−4660.

(18) Jang, Y. J.; Jang, J. W.; Choi, S. H.; Kim, J. Y.; Kim, J. H.; Youn, D. H.; Kim, W. Y.; Han, S.; Sung Lee, J. Tree branch-shaped cupric oxide for highly effective photoelectrochemical water reduction. *Nanoscale* **2015**, *7* (17), 7624−7631.

(19) Chiang, C. Y.; Epstein, J.; Brown, A.; Munday, J. N.; Culver, J. N.; Ehrman, S. Biological templates for antireflective current collectors for photoelectrochemical cell applications. *Nano Lett.* **2012**, *12* (11), 6005−6011.

(20) Paracchino, A.; Laporte, V.; Sivula, K.; Gratzel, M.; Thimsen, E. Highly active oxide photocathode for photoelectrochemical water reduction. *Nat. Mater.* **2011**, *10* (6), 456−461.

(21) Paracchino, A.; Mathews, N.; Hisatomi, T.; Stefik, M.; Tilley, S. D.; Grätzel, M. Ultrathin films on copper(i) oxide water splitting photocathodes: a study on performance and stability. *Energy Environ. Sci.* **2012**, *5* (9), 8673.

(22) Paracchino, A.; Brauer, J. C.; Moser, J.-E.; Thimsen, E.; Graetzel, M. Synthesis and Characterization of High-Photoactivity Electrodeposited Cu_2O Solar Absorber by Photoelectrochemistry and Ultrafast Spectroscopy. *J. Phys. Chem. C* **2012**, *116* (13), 7341−7350.

(23) Prevot, M. S.; Guijarro, N.; Sivula, K. Enhancing the Performance of a robust sol-gel-processed p-type delafossite $CuFeO_2$ photocathode for solar water reduction. *ChemSusChem* **2015**, *8* (8), 1359−1367.

(24) Read, C. G.; Park, Y.; Choi, K. S. Electrochemical Synthesis of p-Type $CuFeO_2$ Electrodes for Use in a Photoelectrochemical Cell. *J. Phys. Chem. Lett.* **2012**, *3* (14), 1872−1876.

(25) Jang, Y. J.; Park, Y. B.; Kim, H. E.; Choi, Y. H.; Choi, S. H.; Lee, J. S. Oxygen-Intercalated $CuFeO_2$ Photocathode Fabricated by Hybrid Microwave Annealing for Efficient Solar Hydrogen Production. *Chem. Mater.* **2016**, *28* (17), 6054−6061.

(26) Kang, D.; Hill, J. C.; Park, Y.; Choi, K.-S. Photoelectrochemical Properties and Photostabilities of High Surface Area $CuBi_2O_4$ and Ag-Doped $CuBi_2O_4$ Photocathodes. *Chem. Mater.* **2016**, *28* (12), 4331−4340.

(27) Cao, D.; Nasori, N.; Wang, Z.; Mi, Y.; Wen, L.; Yang, Y.; Qu, S.; Wang, Z.; Lei, Y. p-Type $CuBi_2O_4$ an easily accessible photocathodic material for high-efficiency water splitting. *J. Mater. Chem. A* **2016**, *4* (23), 8995−9001.

(28) Sahoo, P. P.; Zoellner, B.; Maggard, P. A. Optical, electronic, and photoelectrochemical properties of the p-type $Cu_{3-x}VO_4$ semiconductor. *J. Mater. Chem. A* **2015**, *3* (8), 4501−4509.

(29) Kormányos, A.; Thomas, A.; Huda, M. N.; Sarker, P.; Liu, J. P.; Poudyal, N.; Janáky, C.; Rajeshwar, K. Solution Combustion Synthesis, Characterization, and Photoelectrochemistry of $CuNb_2O_6$ and $ZnNb_2O_6$ Nanoparticles. *J. Phys. Chem. C* **2016**, *120* (29), 16024−16034.

(30) Zhao, W.; Jin, Y.; Gao, C. H.; Gu, W.; Jin, Z. M.; Lei, Y. L.; Liao, L. S. A simple method for fabricating p−n junction photocatalyst $CuFe_2O_4/Bi_4Ti_3O_{12}$ and its photocatalytic activity. *Mater. Chem. Phys.* **2014**, *143* (3), 952−962.

(31) Helaïli, N.; Bessekhouad, Y.; Bachari, K.; Trari, M. Synthesis and physical properties of the $CuFe_{2-x}Mn_xO_4$ ($0 \leq x \leq 2$) solid solution. *Mater. Chem. Phys.* **2014**, *148* (3), 734−743.

(32) Diez-Garcia, M. I.; Lana-Villarreal, T.; Gomez, R. Study of Copper Ferrite as a Novel Photocathode for Water Reduction: Improving Its Photoactivity by Electrochemical Pretreatment. *ChemSusChem* **2016**, *9*, 1504−1512.
(33) Dillert, R.; Taffa, D. H.; Wark, M.; Bredow, T.; Bahnemann, D. W. Research Update: Photoelectrochemical water splitting and photocatalytic hydrogen production using ferrites (MFe_2O_4) under visible light irradiation. *APL Mater.* **2015**, *3* (10), 104001.
(34) Chen, Z.; Jaramillo, T. F.; Deutsch, T. G.; Kleiman-Shwarsctein, A.; Forman, A. J.; Gaillard, N.; Garland, R.; Takanabe, K.; Heske, C.; Sunkara, M.; et al. Accelerating materials development for photoelectrochemical hydrogen production: Standards for methods, definitions, and reporting protocols. *J. Mater. Res.* **2010**, *25* (01), 3−16.
(35) Saadi, S.; Bouguelia, A.; Trari, M. Photoassisted hydrogen evolution over spinel CuM_2O_4 (M = Al, Cr, Mn, Fe and Co). *Renewable Energy* **2006**, *31* (14), 2245−2256.
(36) Li, X.; Liu, A.; Chu, D.; Zhang, C.; Du, Y.; Huang, J.; Yang, P. High Performance of Manganese Porphyrin Sensitized p-Type $CuFe_2O_4$ Photocathode for Solar Water Splitting to Produce Hydrogen in a Tandem Photoelectrochemical Cell. *Catalysts* **2018**, *8* (3), 108.
(37) Kezzim, A.; Nasrallah, N.; Abdi, A.; Trari, M. Visible light induced hydrogen on the novel hetero-system $CuFe_2O_4/TiO_2$. *Energy Convers. Manage.* **2011**, *52* (8−9), 2800−2806.
(38) Kim, J. K.; Chai, S. U.; Cho, Y.; Cai, L.; Kim, S. J.; Park, S.; Park, J. H.; Zheng, X. Ultrafast Flame Annealing of TiO_2 Paste for Fabricating Dye-Sensitized and Perovskite Solar Cells with Enhanced Efficiency. *Small* **2017**, *13* (42), 1702260.
(39) Feng, Y.; Cho, I. S.; Rao, P. M.; Cai, L.; Zheng, X. Sol-flame synthesis: a general strategy to decorate nanowires with metal oxide/noble metal nanoparticles. *Nano Lett.* **2013**, *13* (3), 855−860.
(40) Cai, L.; Cho, I. S.; Logar, M.; Mehta, A.; He, J.; Lee, C. H.; Rao, P. M.; Feng, Y.; Wilcox, J.; Prinz, F. B.; et al. Sol-flame synthesis of cobalt-doped TiO_2 nanowires with enhanced electrocatalytic activity for oxygen evolution reaction. *Phys. Chem. Chem. Phys.* **2014**, *16* (24), 12299−12306.
(41) Kang, B. K.; Han, G. S.; Baek, J. H.; Lee, D. G.; Song, Y. H.; Kwon, S. B.; Cho, I. S.; Jung, H. S.; Yoon, D. H. Nanodome Structured $BiVO_4/GaO_xN_{1-x}$ Photoanode for Solar Water Oxidation. *Adv. Mater. Interfaces* **2017**, *4* (17), 1700323.
(42) Qiu, Y.; Liu, W.; Chen, W.; Chen, W.; Zhou, G.; Hsu, P.-C.; Zhang, R.; Liang, Z.; Fan, S.; Zhang, Y.; Cui, Y. Efficient solar-driven water splitting by nanocone $BiVO_4$-perovskite tandem cells. *Sci. Adv.* **2016**, *2*, No. e1501764.
(43) Wang, W.; Zhang, Y.; Wang, L.; Bi, Y. Facile synthesis of Fe^{3+}/Fe^{2+} self-doped nanoporous $FeVO_4$ photoanodes for efficient solar water splitting. *J. Mater. Chem. A* **2017**, *5* (6), 2478−2482.
(44) Shi, X.; Cai, L.; Ma, M.; Zheng, X.; Park, J. H. General Characterization Methods for Photoelectrochemical Cells for Solar Water Splitting. *ChemSusChem* **2015**, *8* (19), 3192−3203.
(45) Annamalai, A.; Subramanian, A.; Kang, U.; Park, H.; Choi, S. H.; Jang, J. S. Activation of Hematite Photoanodes for Solar Water Splitting: Effect of FTO Deformation. *J. Phys. Chem. C* **2015**, *119* (7), 3810−3817.
(46) Kim, J. Y.; Magesh, G.; Youn, D. H.; Jang, J. W.; Kubota, J.; Domen, K.; Lee, J. S. Single-crystalline, wormlike hematite photoanodes for efficient solar water splitting. *Sci. Rep.* **2013**, *3*, 2681.
(47) Krishnan, V.; Selvan, R. K.; Augustin, C. O.; Gedanken, A.; Bertagnolli, H. EXAFS and XANES Investigations of $CuFe_2O_4$ Nanoparticles and $CuFe_2O_4-MO_2$ (M = Sn, Ce) Nanocomposites. *J. Phys. Chem. C* **2007**, *111* (45), 16724−16733.
(48) Wong, J.; Lytle, F. W.; Messmer, R. P.; Maylotte, D. H. K-edge absorption spectra of selected vanadium compounds. *Phys. Rev. B: Condens. Matter Mater. Phys.* **1984**, *30* (10), 5596−5610.
(49) Caddeo, F.; Loche, D.; Casula, M. F.; Corrias, A. Evidence of a cubic iron sub-lattice in t-$CuFe_2O_4$ demonstrated by X-ray Absorption Fine Structure. *Sci. Rep.* **2018**, *8* (1), 797.
(50) Xiao, Z.; Wang, Y.; Huang, Y.-C.; Wei, Z.; Dong, C.-L.; Ma, J.; Shen, S.; Li, Y.; Wang, S. Filling the oxygen vacancies in Co_3O_4 with phosphorus: an ultra-efficient electrocatalyst for overall water splitting. *Energy Environ. Sci.* **2017**, *10* (12), 2563−2569.
(51) Lopes, T.; Andrade, L.; Le Formal, F.; Gratzel, M.; Sivula, K.; Mendes, A. Hematite photoelectrodes for water splitting: evaluation of the role of film thickness by impedance spectroscopy. *Phys. Chem. Chem. Phys.* **2014**, *16* (31), 16515−16523.
(52) Xia, T.; Zhang, Y.; Murowchick, J.; Chen, X. Vacuum-treated titanium dioxide nanocrystals: Optical properties, surface disorder, oxygen vacancy, and photocatalytic activities. *Catal. Today* **2014**, *225*, 2−9.
(53) Benck, J. D.; Chen, Z.; Kuritzky, L. Y.; Forman, A. J.; Jaramillo, T. F. Amorphous Molybdenum Sulfide Catalysts for Electrochemical Hydrogen Production: Insights into the Origin of their Catalytic Activity. *ACS Catal.* **2012**, *2* (9), 1916−1923.
(54) Tilley, S. D.; Schreier, M.; Azevedo, J.; Stefik, M.; Graetzel, M. Ruthenium oxide hydrogen evolution catalysis on composite cuprous oxide water splitting photocathodes. *Adv. Funct. Mater.* **2014**, *24*, 303−311.
(55) Dubale, A. A.; Tamirat, A. G.; Chen, H.-M.; Berhe, T. A.; Pan, C.-J.; Su, W.-N.; Hwang, B.-J. A highly stable CuS and CuS−Pt modified Cu_2O/CuO heterostructure as an efficient photocathode for the hydrogen evolution reaction. *J. Mater. Chem. A* **2016**, *4* (6), 2205−2216.